



HAL
open science

Innovative synthesis of mesostructured CoSb₃-based skutterudites by magnesio-reduction

S. Le Tonquesse, E Alleno, Valérie Demange, V. Dorcet, Loïc Joanny, C. Prestipino, O. Rouleau, M. Pasturel

► To cite this version:

S. Le Tonquesse, E Alleno, Valérie Demange, V. Dorcet, Loïc Joanny, et al.. Innovative synthesis of mesostructured CoSb₃-based skutterudites by magnesio-reduction. *Journal of Alloys and Compounds*, 2019, 796, pp.176-184. 10.1016/j.jallcom.2019.04.324 . hal-02161323

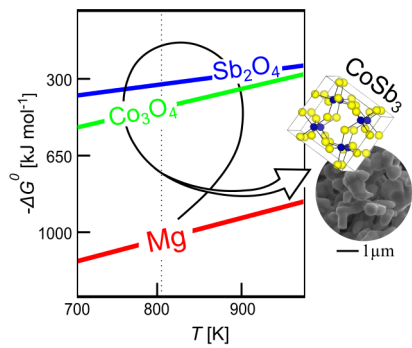
HAL Id: hal-02161323

<https://univ-rennes.hal.science/hal-02161323>

Submitted on 1 Jul 2019

HAL is a multi-disciplinary open access archive for the deposit and dissemination of scientific research documents, whether they are published or not. The documents may come from teaching and research institutions in France or abroad, or from public or private research centers.

L'archive ouverte pluridisciplinaire **HAL**, est destinée au dépôt et à la diffusion de documents scientifiques de niveau recherche, publiés ou non, émanant des établissements d'enseignement et de recherche français ou étrangers, des laboratoires publics ou privés.



Innovative synthesis of mesostructured CoSb₃-based skutterudites by magnesioreduction

Sylvain Le Tonquesse^a, Éric Alleno^b, Valérie Demange^a, Vincent Dorcet^a, Loic Joanny^a, Carmelo Prestipino^a, Olivier Rouleau^b, Mathieu Pasturel^a*

^aUniv Rennes, CNRS, ISCR-UMR6226/ScanMAT-UMS2001, F-35000, Rennes, France

^bUniversité Paris-Est, Institut de Chimie et des Matériaux Paris-Est, UMR 7182 CNRS - UPEC, 2 rue H. Dunant, 94320 THIAIS, France

Abstract

High purity CoSb₃, Ni_{0.06}Co_{0.94}Sb₃ and In_{0.13}Co₄Sb₁₂ were synthesized from oxides by magnesioreduction. This novel synthesis route to CoSb₃-based skutterudites directly yields highly crystalline powders with submicronic grain size. Densified mesostructured pellets with an average grain size ranging between 550 and 800 nm were obtained by spark plasma sintering. The strong phonon scattering induced by the mesostructuration leads to a lattice thermal conductivity reduction up to 25 % for CoSb₃ and Ni_{0.06}Co_{0.94}Sb₃ at 300 K without significantly degrading the electronic properties. Consequently, maximum *ZT* figures-of-merit of 0.09, 0.60 and 0.75 are found for CoSb₃, Ni_{0.06}Co_{0.94}Sb₃ and In_{0.13}Co₄Sb₁₂, respectively, showing the ability of this scalable process to reach the best performances reported in literature for these compositions at moderate temperature and annealing duration.

Keywords: Intermetallics; Thermoelectric materials; Chemical synthesis; Powder metallurgy; Microstructure

*mathieu.pasturel@univ-rennes1.fr

1. Introduction

Thermoelectric materials (TM) enable the direct conversion of a temperature gradient into voltage, thus offering the opportunity to directly exchange wasted heat into electricity by highly reliable solid state power generators. However, TM-based technologies are still only used in niche applications because of the low performances, high cost or complex synthesis of the currently available materials [1]. Among them, CoSb₃-based skutterudites have attracted great attention as promising mid-temperature TM due to their high power factor $PF = \alpha^2/\rho$ (where α is the Seebeck coefficient and ρ the electrical resistivity), good mechanical properties and relatively abundant constituting chemical elements [2, 3, 4, 5]. However its thermal conductivity κ is high - up to $9 \text{ W m}^{-1} \text{ K}^{-1}$ at 293 K in polycrystalline CoSb₃ [6] - mainly due to the lattice (phonon) contribution κ_L and much less to the charge carrier contribution κ_e , with $\kappa = \kappa_L + \kappa_e$.

Any attempt to improve the dimensionless thermoelectric figure-of-merit ZT , defined as:

$$ZT = \frac{\alpha^2}{\rho(\kappa_L + \kappa_e)} T \quad (1)$$

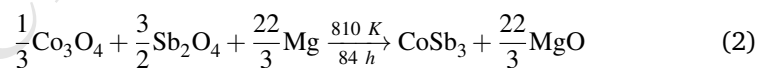
in CoSb₃ involves (i) the optimization of PF by adjusting the carrier concentration in the semiconducting material and (ii) the reduction of κ_L . The latter can be achieved by creating phonon scattering centers at different length scales in the materials:

(i) At the atomic scale, the most common strategy consists in partially filling the icosahedral $2a$ crystallographic position of skutterudite structure with heavy atoms. The low energy phonons introduced by the filler atom as well as the mass fluctuation arising from its random occupancy both scatter the heat carrying phonons resulting in a strongly reduced κ_L [7, 8, 9, 10]. Chemical doping on the Co- or Sb-sublattice, which is necessary to achieve optimal charge carrier concentration, has also been shown to affect the thermal conductivity via the mass fluctuation phenomenon [11, 12].

29 (ii) At the microstructural scale, grain boundaries in bulk polycrystalline ma-
 30 terials also act as effective phonon-scattering centers [13, 14]. Their effect is
 31 highly intensified in nano- or mesostructured materials where κ_L can be reduced
 32 by more than 35 % compared to identical materials with much larger grain
 33 size [15, 16]. As a result, it stimulates the development of alternative synthe-
 34 sis routes more suitable for the production of submicronic powders than tradi-
 35 tional melting-annealing methods, such as ball-milling / spark plasma sintering
 36 (SPS) [17, 18], severe plastic deformation [19], melt spinning [20, 21], com-
 37 bustion synthesis [22], flash-spark plasma sintering [23], high-pressure synthe-
 38 ses [24, 25], gas atomization [26] or solution proceed [27, 28]. Improvement
 39 of ZT by this approach can only be realized if the decrease of κ is not counter-
 40 balanced by a decrease of PF due to overly enhanced electron scattering at the
 41 grain boundaries.

42 Phonons being more likely scattered by defects with sizes close to their wave-
 43 lengths, the creation of defects at different length scales in the material, often
 44 refereed as ‘all-scale hierarchical architectures’, offers the possibility to scat-
 45 ter phonons over a broader energy spectrum, thus reducing κ more efficiently
 46 [1, 29, 30, 31]. Very recently, this multi-scale approach have been success-
 47 fully employed with nanostructured filled-skutterudites [32, 33], porous doped-
 48 skutterudites [34, 35] or formation of nanoinclusions in filled- and doped-
 49 skutterudites [36, 37].

50 With this approach in mind, we developed the magnesio-reduction synthesis
 51 of pristine, Ni-doped and In-filled CoSb_3 according to the reaction:



52 This new synthesis route to CoSb_3 -based skutterudites, inspired from indus-
 53 trial pyrometallurgical processes (*e.g.* Kroll’s process), yields powders with sub-
 54 micronic grain size that can be readily used for the sintering of mesostructured
 55 densified materials [38]. It offers other advantages such as the use of air stable
 56 and cheap oxides as precursors, relatively low temperature and short reaction

57 time compared to conventional melting/annealing synthesis, good control of the
58 chemical composition and high yield. In this article, the structural, microstruc-
59 tural and thermoelectric characterizations of these materials are reported and
60 compared to literature data on similar materials (either mesostructured or not)
61 prepared by conventional synthesis routes.

62 **2. Experimental procedures**

63 **2.1. Synthesis of CoSb_3 by magnesioreduction**

64 The first step of the synthesis consists in the preparation of an intimate mixture
65 of Co_3O_4 (Sigma-Aldrich, 99.9 %) and Sb_2O_4 (Sigma-Aldrich, 99.995 %) with a
66 molar ratio of 1:5.4 (20 % excess of Sb_2O_4) by thoroughly grinding the powders
67 together in a vibrating mill (Retsch MM200) for 20 min at 25 Hz using tungsten
68 carbide vial and ball. The oxide mixture was then cold-pressed at 250 MPa into
69 \varnothing 10 mm pellets with approximately 2 mm height. Two pellets were stacked
70 together on top of a Mg chips bed (Strem, ≥ 99 %) lying at the bottom of a
71 Mo crucible (Fig. 1). The quantity of Mg needed to complete the reduction
72 was determined from the masses of Co_3O_4 and Sb_2O_4 to be reduced plus an
73 additional 2-3 % excess. The Mo crucible is then closed and placed in an argon-
74 filled Inconel tube to prevent its oxidation during the thermal process. The
75 reactor was heated up to 810 K at 100 K h^{-1} and held at this temperature for
76 84 h before being cooled down to room temperature. After the reaction, CoSb_3
77 remains in the shape of compact pellets and could easily be separated from the
78 loose MgO. The powders were spark plasma sintered (FCT HP-D-10 system) in
79 \varnothing 10 mm graphite dies at 910 K and 66 MPa for 5 min with heating/cooling
80 ramps of 100 K min^{-1} .

81 **2.2. Synthesis of $\text{Ni}_{0.06}\text{Co}_{0.94}\text{Sb}_3$ and $\text{In}_{0.13}\text{Co}_4\text{Sb}_{12}$ by magne- 82 **sioreduction****

83 The synthesis of Ni-doped and In-inserted CoSb_3 was attempted from a mixture
84 of cobalt, nickel/indium and antimony oxides. Nevertheless, the primary for-

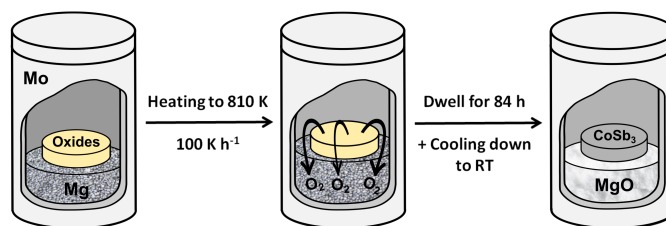


Fig. 1: Experimental procedure for the synthesis of CoSb_3 -based skutterudites by magnesio-reduction of the corresponding (un-)doped Co_3O_4 and Sb_2O_4 oxide precursors (yellow pellet). See text for details.

85 mation of NiSb_2 and InSb during the magnesio-reduction process did not allow
 86 to obtain pure samples in relatively fast and low temperature conditions. Mixed
 87 precursor oxides were thus prepared in order to start from an intimate mixture
 88 of metallic ions to speed up the process.

89 For the preparation of $\text{Ni}_{0.18}\text{Co}_{2.82}\text{O}_4$ precursor, $\text{Co}(\text{NO}_3)_2 \cdot 6\text{H}_2\text{O}$ (Fluka, \geq
 90 98%) and $\text{Ni}(\text{NO}_3)_2 \cdot 6\text{H}_2\text{O}$ (Fluka, \geq 99%) were dissolved in distilled water
 91 with a molar ratio of about 16:1. The solution was stirred for 30 min and
 92 evaporated at 363 K. The slurry was ground before being decomposed in air at
 93 573 K for 4 h leading to the formation of a black powder. The Bragg peaks of
 94 the X-ray diffraction (XRD) patterns correspond to the Co_3O_4 structure ($Fd\bar{3}m$)
 95 with lattice parameter $a = 8.0905(5) \text{ \AA}$ (Fig. SI.1), suggesting the insertion
 96 of Ni in Co_3O_4 ($a \approx 8.086 \text{ \AA}$). Accordingly, the metal ratio determined by X-ray
 97 energy dispersive spectroscopy (EDS) is in good agreement with the expected
 98 $\text{Ni}_{0.18}\text{Co}_{2.82}\text{O}_4$ composition.

99 For the preparation of $\text{In}_{0.10}\text{Co}_{2.90}\text{O}_4$ precursor, $\text{CoCl}_2 \cdot 6\text{H}_2\text{O}$ (Prolabo, 99.9 %)
 100 and $\text{In}(\text{NO}_3)_3 \cdot x\text{H}_2\text{O}$ (home made by dissolving metallic indium in concentrated
 101 nitric acid) were dissolved in distilled water with a molar ratio of about 29:1
 102 under vigorous stirring. Then a suitable amount (+20 % excess) of NaOH was
 103 added to form the metal hydroxides. The blue precipitate was then centrifuged,
 104 washed with water and ethanol, dried overnight at about 363 K and calcinated
 105 at 723 K to obtain the corresponding oxide. Powder XRD pattern (Fig. SI.2)
 106 shows broad diffraction peaks corresponding to the Co_3O_4 structure. Le Bail

107 refinement of the experimental pattern nevertheless converges to a cell param-
108 eter $a = 8.102(7) \text{ \AA}$ which could indicate the insertion of In on the Co-lattice
109 in agreement with recent results by Ma *et al.* [39].

110 From these $\text{Ni}_{0.18}\text{Co}_{2.82}\text{O}_4$ and $\text{In}_{0.10}\text{Co}_{2.90}\text{O}_4$ precursors, $\text{Ni}_{0.06}\text{Co}_{0.94}\text{Sb}_3$ and
111 $\text{In}_{0.13}\text{Co}_4\text{Sb}_{12}$ were synthesized using the same procedure as for CoSb_3 , at iden-
112 tical temperature and duration.

113 These compositions have been selected as (i) the optimized carrier concen-
114 tration for Ni-doped sample [40, 41] and as (ii) a composition close to those
115 usually presented in articles dealing with In-inserted skutterudites [42, 43, 44,
116 45, 46, 47].

117 2.3. Materials characterization

118 The crystal structure and purity of the samples were checked by powder XRD us-
119 ing a Bruker D8 Advance diffractometer in the Bragg-Brentano geometry work-
120 ing with a monochromatized $\text{Cu K}\alpha_1$ radiation ($\lambda = 1.5406 \text{ \AA}$). The diffractome-
121 ter is equipped with a 1D LynxEye detector with a photon energy discrimina-
122 tion around 20 % thus reducing the cobalt fluorescence signal. Lattice constants
123 were determined by Le Bail refinements as implemented in the FullProf Suite
124 software [48].

125 Scanning electron microscopy (SEM) images, energy dispersive spectroscopy
126 (EDS) and electron backscattering diffraction (EBSD) were performed using a
127 JEOL JSM 7100 F microscope equipped with an Oxford EDS SDD X-Max spec-
128 trometer and an EBSD HKL Advanced Nordlys Nano detector. Preparation of
129 the powder samples for SEM analyses consisted in a mere deposition on carbon
130 tape followed by metallization with carbon. As for the densified samples, the
131 pellets were successively polished with SiC, diamond paste and colloidal silica
132 and pasted on SEM holders using silver lacquer. Samples for the transmission
133 electron microscopy were first thinned by dimpling with colloidal silica and then
134 by Ar ion milling using a Fischione Ion Mill 1010 operating at 4.5 kV and 5 mA.
135 Transmission electron microscopy (TEM) analyses were performed on a JEOL
136 2100 LaB₆ instrument operating at 200 kV and equipped with a high resolution

137 Gatan US1000 camera, and an Orius 200D camera.

138 The Seebeck coefficient $\alpha(T)$ and electrical resistivity $\rho(T)$ measurements
 139 were realized using a home made apparatus described elsewhere [49]. Thermal
 140 diffusivities were measured in argon atmosphere with the laser flash method us-
 141 ing a Netzsch LFA 457 equipment. The total thermal conductivity κ was deter-
 142 mined by multiplying the thermal diffusivity, the specific heat calculated from
 143 the Dulong-Petit law and the experimental density of the samples.

144 3. Results and discussion

145 3.1. Structural and microstructural characterization of as-synthesized 146 and SPSed materials

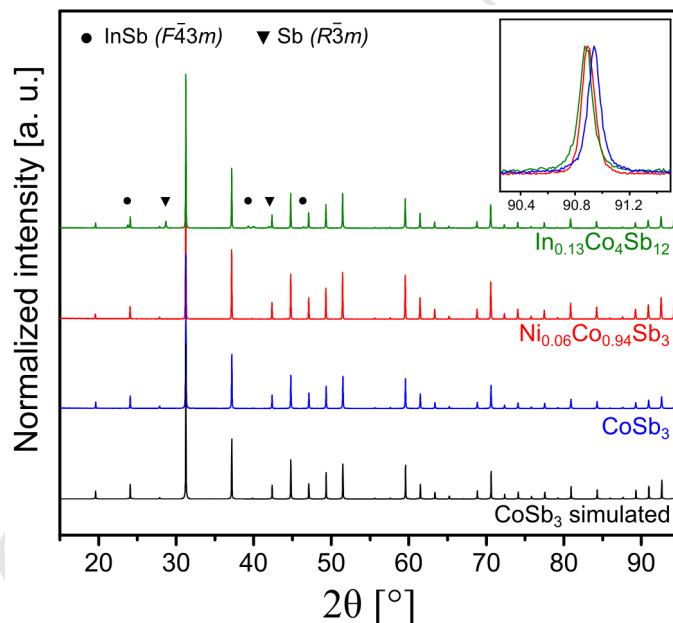


Fig. 2: Experimental XRD patterns of the as-synthesized skutterudite powders and theoretical one calculated with FullProf [48] from cell parameters and atomic positions given in [50] and peak profile function from the utilized diffractometer. The inset shows the shift of the (653) diffraction peak of the CoSb_3 structure (systematic peak shift due to sample displacement is corrected) revealing the lattice parameter evolution among the samples.

147 The powder XRD patterns of pristine and Ni-doped CoSb_3 (Fig. 2) are fully

148 indexed according to the skutterudite structure, revealing a single phase prod-
149 uct. Only few traces of InSb ($F\bar{4}3m$) and Sb ($R\bar{3}m$) are visible on the XRD pattern
150 of the indium containing compound. Le Bail fitting of the XRD patterns results
151 in cell parameters of $a = 9.0350(2)$, $9.0434(1)$ and $9.0443(6)$ Å for CoSb_3 ,
152 $\text{Ni}_{0.06}\text{Co}_{0.94}\text{Sb}_3$ and ' $\text{In}_{0.13}\text{Co}_4\text{Sb}_{12}$ ', respectively, indicating an effective substitu-
153 tion by nickel on the cobalt site and insertion of indium in the cages of the struc-
154 ture [44, 51, 52]. By comparison with literature data, one can expect chemical
155 compositions close to $\text{Ni}_{0.06}\text{Co}_{0.94}\text{Sb}_3$ and $\text{In}_{0.10}\text{Co}_4\text{Sb}_{12}$ from these lattice pa-
156 rameter values [40, 53]. The discrepancy with the targeted In-concentration
157 could be explained by some residual InSb binary compound in the sample. The
158 diffraction peaks exhibit very narrow profiles characteristic of well-crystallized
159 matter which may favor the electrical transport in these materials. Surprisingly,
160 no traces of MgO are visible on these patterns which is quite unusual for such a
161 process [54, 55, 56] and may result either from the absence of this by-product
162 or from its amorphous nature, the reaction being carried out at a relatively low
163 temperature.

164 SEM examination of the obtained powders reveals faceted submicronic grains
165 (Fig. 3). The grain size ranges from 300 nm to 1 μm for CoSb_3 and its Ni-
166 doped counterpart and from 100 nm to 1 μm for the In-inserted skutterudite.
167 Such small particles are required to lower the thermal conductivity and are usu-
168 ally obtained by high energy ball-milling with both risks of contamination from
169 the milling material and decomposition of the phase. In agreement with the
170 narrow XRD peaks, the shape of most of the grains clearly indicates their sin-
171 gle crystalline nature. EDS analyses of the Ni-doped CoSb_3 powders confirm
172 the presence of Ni in the sample with a concentration of ≈ 1 at.%. On the
173 other hand, no characteristic X-ray emission peaks of In could be detected for
174 the filled skutterudite and this could be explained by the low concentration of
175 the element in the material (< 1 at.%) being below the detection limit of the
176 technique. No signal of Mg is visible on the X-ray emission spectra from all the
177 samples.

178 Both XRD and EDS analyses indicate the absence of MgO in the as-synthesized

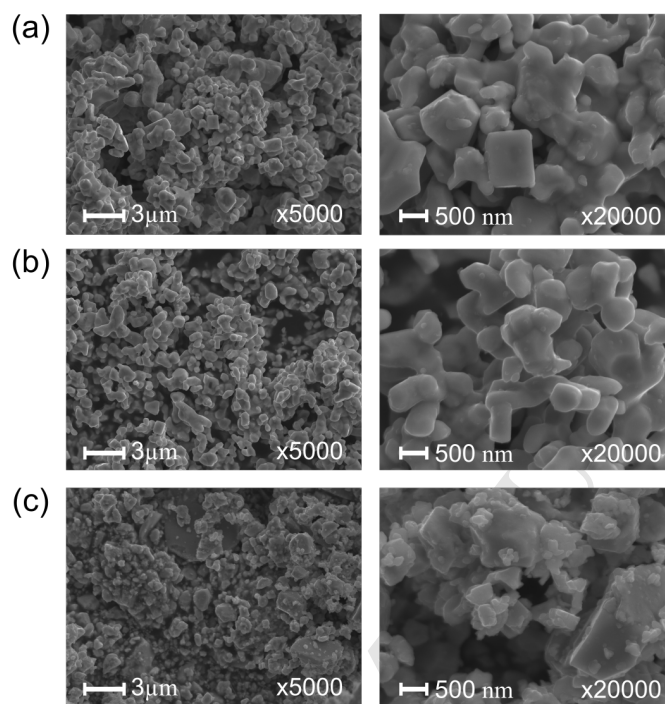


Fig. 3: Secondary electron SEM images of the as-synthesized (a) CoSb_3 (b) $\text{Ni}_{0.06}\text{Co}_{0.94}\text{Sb}_3$ and (c) $\text{In}_{0.13}\text{Co}_4\text{Sb}_{12}$ at two different magnifications.

179 products. In addition, TEM observations coupled with EDS analyses did not
 180 reveal any traces of Mg or MgO particles in the samples. Together with the re-
 181 tention of both mixed-oxide pellet and magnesium turning shapes, and based
 182 on the Ellingham diagram [57] for the metals in presence, we hypothesize
 183 solid-gas driven reduction reactions at 810 K: Mg consumes the residual O_2
 184 atmosphere in the crucible ($p_{eq}(\text{O}_2) = 10^{-63}$ Pa) inducing the decomposition of
 185 Co_3O_4 ($p_{eq}(\text{O}_2) = 10^{-19}$ Pa) and Sb_2O_4 ($p_{eq}(\text{O}_2) = 10^{-14}$ Pa) into native metals
 186 that readily react together to form the skutterudite phase.

187 Spark plasma sintering was used to prepare the skutterudite pellets because
 188 it can achieve high densities in short sintering times thus limiting grain growth
 189 during the densification process. With the sintering conditions given in 2.1,
 190 relative densities ranging from 96 to 97 % were obtained (Table 1).

191 Le Bail fitting of the XRD patterns measured on sintered pellets polished

192 surfaces (Fig. 4 and SI.4) do not show significant evolution of the unit cell
 193 parameter for CoSb_3 and $\text{Ni}_{0.06}\text{Co}_{0.94}\text{Sb}_3$ ($a = 9.0361(2)$ and $9.0428(1)$ Å,
 194 respectively). A significant increase up to $a = 9.0482(3)$ Å is observed for
 195 $\text{In}_{0.13}\text{Co}_4\text{Sb}_{12}$, which, together with the disappearance of the InSb Bragg peaks,
 196 is attributed to a higher insertion of indium in the cages available in the skutterudite
 197 structure. Considering the low melting point (789 K) reported for InSb
 198 [58], its reactivity with the skutterudite matrix during the sintering process per-
 199 formed above this melting point was expected. Only a very small amount of
 200 antimony ($R\bar{3}m$) could be detected by XRD after sintering and it was found to
 201 represent less than 1 wt.% of the sample. The latter cell parameter corresponds
 202 to the composition $\text{In}_x\text{Co}_4\text{Sb}_{12}$ with $0.13 \leq x \leq 0.15$, depending on the literature
 203 data [42, 53].

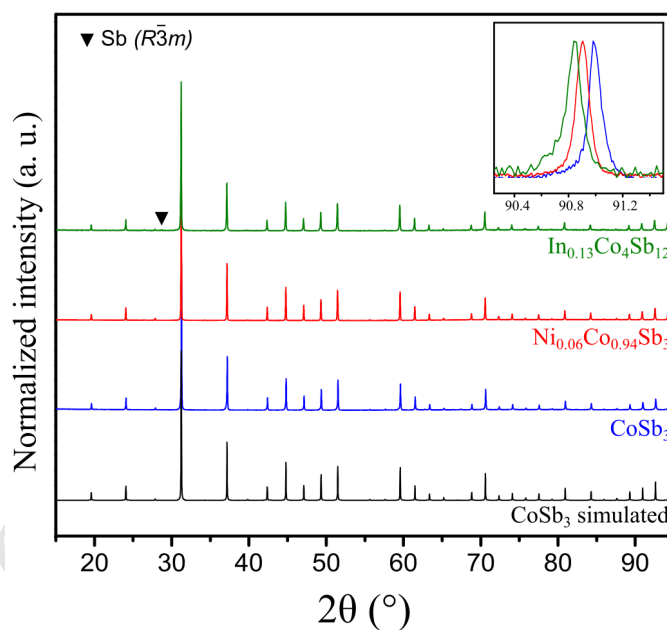


Fig. 4: Experimental XRD patterns of the sintered skutterudite pellets and theoretical one calculated with FullProf [48] from cell parameters and atomic positions given in [50] and peak profile function from the utilized diffractometer. The inset shows the shift of the (653) diffraction peak of the CoSb_3 structure (systematic peak shift due to sample displacement is corrected) revealing the lattice parameter evolution among the samples.

204 SEM-EDS analyses performed on several spots of the polished surfaces gives

205 a mean Ni concentration of 1.5 at.% for the Ni-doped samples, which is in good
 206 agreement with the targeted and crystallographic compositions. This composi-
 207 tion is homogeneous through the analyzed polished surface and no concentra-
 208 tion gradient is observed. As for the powders, no significant In or Mg content
 209 could be detected on any samples by EDS analyses which means that those ele-
 210 ments are in concentration below the detection limit of the technique.

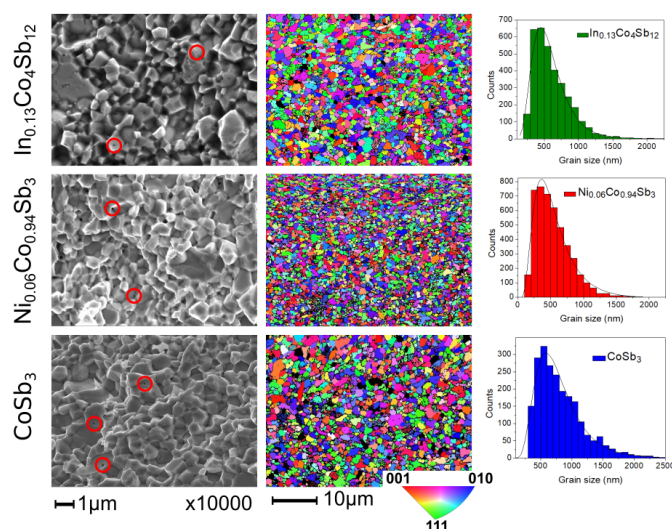


Fig. 5: Secondary electron SEM images of the pellet cross-sections (left) showing some residual porosity (circled in red). EBSD mappings (middle) of the polished pellet surfaces and histograms (right) showing the distribution of grain sizes determined from EBSD maps for the SPSeD CoSb_3 (bottom), $\text{Ni}_{0.06}\text{Co}_{0.94}\text{Sb}_3$ (middle) and $\text{In}_{0.13}\text{Co}_4\text{Sb}_{12}$ (top) skutterudites.

211 In order to check how sintering affects grain size, electron backscattering
 212 diffraction (EBSD) and SEM imaging (Fig. 5) were performed on polished sur-
 213 faces and on broken cross-sections of the pellets, respectively. SEM imaging
 214 reveals some closed porosity (encircled in red) which is responsible for the full
 215 densification deviation. EBSD mappings were realized on a $1750.5 \pm 9.5 \mu\text{m}^2$
 216 area with a step size of 100 nm for CoSb_3 and $\text{In}_{0.13}\text{Co}_4\text{Sb}_{12}$ and 50 nm for
 217 $\text{Ni}_{0.06}\text{Co}_{0.94}\text{Sb}_3$ to distinguish better smaller grains. Kikuchi lines were well in-
 218 dexed using the skutterudite structure and cell parameters obtained from XRD,
 219 and only a few non-indexed areas were found on the 3 pellets. First of all, one

220 can notice a random distribution of the grains orientation throughout the ana-
 221 lyzed areas. Then submicronic particles are found to cover the majority of the
 222 surface in all cases, with apparent smaller sizes for the Ni-doped antimonide
 223 compared to the other two compounds.

Table 1: Summary of the main structural and microstructural features of the sintered skutterudite pellets used for the thermoelectric characterizations

Nominal composition	a [Å]	Impurity [wt.%]	Average grain size [nm]	Relative density [%]
CoSb ₃	9.0362(4)	None	784 ± 376	96
Ni _{0.06} Co _{0.94} Sb ₃	9.0428(3)	None	580 ± 336	97
In _{0.13} Co ₄ Sb ₁₂	9.0482(3)	Sb (<1)	617 ± 292	97

224 In order to quantify these observations, image analyses were performed us-
 225 ing the *Channel 5* software (HKL Technology) by considering all the diffracting
 226 domains containing at least 7 pixels (*i.e.* $\sim 0.07 \mu\text{m}^2$) for CoSb₃ and In_{0.13}Co₄Sb₁₂
 227 and at least 14 pixels (*i.e.* $\sim 0.035 \mu\text{m}^2$) for Ni_{0.06}Co_{0.94}Sb₃. The particles size
 228 distribution (diameter of an equivalent circle with equal surface, Fig. 5) clearly
 229 shows a majority of submicronic particles. This distribution has been fitted us-
 230 ing a log-normal distribution function:

$$f(x) = \frac{A}{x\sigma\sqrt{2\pi}} \cdot \exp\left(-\frac{[\ln(x) - \mu]^2}{2\sigma^2}\right) \quad (3)$$

231 where A , μ and σ are the fitting parameters. From μ and σ values, the average
 232 grain size D and its standard deviation SD can be calculated using the formulae:

$$D = \exp\left(\mu + \frac{\sigma^2}{2}\right) \quad (4)$$

$$SD = \left[(\exp(\sigma^2) - 1) \cdot \exp(2\mu + \sigma^2)\right]^{\frac{1}{2}} \quad (5)$$

233 The average grain sizes are found to range from 780 nm for CoSb₃ down to
 234 580 nm for Ni_{0.06}Co_{0.94}Sb₃ with intermediate values for the In-inserted phase
 235 (Table 1).

236 Such small grain sizes induce numerous grain boundaries, which along the
 237 presence of defects due to crystal orientation mismatches might be efficient to

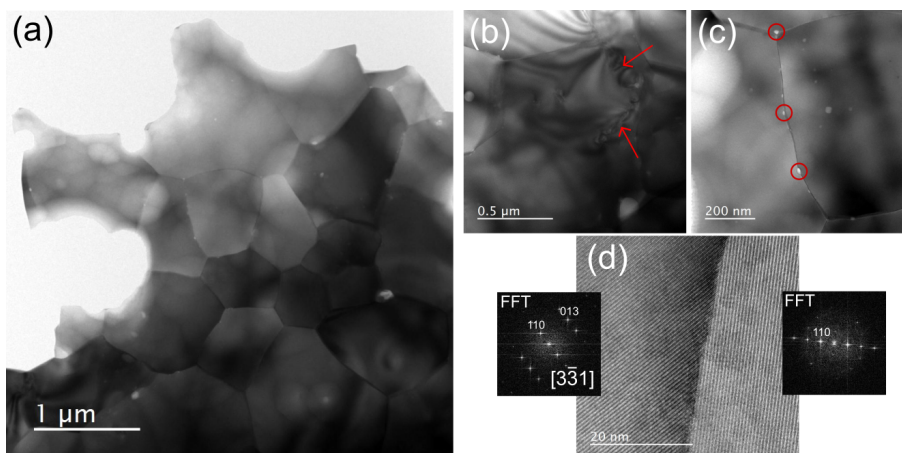


Fig. 6: TEM brightfield images of thinned CoSb_3 sintered pellet. (a) Typical global area, (b) strips indicating lattice distortions originating from dislocations high density at the grain boundaries (red arrows), (c) nano-scale porosities (encircled in red) and (d) HRTEM image showing the crystallinity of the grain boundaries

238 decrease the lattice thermal conductivity. It was shown that dislocations or
 239 nanoscale porosity/precipitate can efficiently reduce the skutterudites thermal
 240 conductivity by phonon scattering [30, 59, 60]. In order to demonstrate the ex-
 241 istence of such defects in our materials, CoSb_3 sintered pellet grains boundaries
 242 have been investigated by TEM. Fig. 6a shows a typical area of the thinned
 243 pellet where the observations were realized. At this magnification, proper tilt-
 244 ing of the sample reveals stripes originating from boundaries and propagating
 245 inside the grains (Fig. 6b). Contrast between those stripes arises from slight
 246 deviation from the diffraction condition and evidences large lattice constraints
 247 in the crystal. These are common to sintered materials as they originate from
 248 high density of dislocations, which are in the present case, mostly located close
 249 to or at the grain boundaries (red arrows). HRTEM examination of such grain
 250 boundaries (Fig. 6d and SI.5) reveals that they are well-crystallized and free
 251 of any amorphous layer. Two major kinds of defects are evidenced in Fig. SI.5
 252 taken on a semi-coherent lattice interface. Typical dislocations appear inside
 253 the grains (Fig. SI.5b) while two dimensional analogues of dislocations [61]
 254 are created at the interface between the grains (Fig. SI.5c), both types being

255 able to scatter mid-wavelength phonons.

256 As shown in Fig. 6c, some porosity with nanometric size (encircled in red)
257 is also observed at the grain boundaries and can also act as efficient phonon
258 scattering centers.

259 All these observations are quite common for sintered materials and are not
260 a special feature resulting from the magnesioreduction synthesis. However, an
261 exacerbated effect on the thermal conductivity is expected in MR-materials be-
262 cause of the high grain boundary concentration leading to an elevated defect
263 concentration.

264

265 **3.2. Thermoelectric characterizations**

266 The electrical resistivities, Seebeck coefficients and thermal conductivities have
267 been determined in the temperature range 300-800 K where skutterudites usu-
268 ally present their maximum ZT value.

269 The electrical resistivity and Seebeck coefficient of the three pellets are
270 shown in Fig. 7a and 7b. CoSb_3 shows a semiconducting shape of $\rho(T)$ in
271 the 300-800 K temperature range and the $\alpha(T)$ evolves from strongly nega-
272 tive at room temperature to positive at 800 K with a sign change at 600 K at-
273 tributed to the intrinsic regime caused by holes activation through the band gap
274 [62, 63, 43]. The electrical resistivity of the Ni-doped and In-inserted skutteru-
275 dites are strongly reduced to respectively 14.5 and 16.0 $\mu\Omega\cdot\text{m}$ at 300 K confirm-
276 ing the insertion of these elements in the crystal structure. The n -doping is con-
277 firmed by the stabilized negative value of $\alpha(T)$ in both cases, ranging between
278 -120 and -200 $\mu\text{V K}^{-1}$ for $\text{Ni}_{0.06}\text{Co}_{0.94}\text{Sb}_3$ and between -180 and -240 $\mu\text{V K}^{-1}$
279 for $\text{In}_{0.13}\text{Co}_4\text{Sb}_{12}$ in the investigated temperature range. The electrical resistivi-
280 ties and Seebeck coefficients are in very good agreement with those reported
281 for similar compositions of Ni-doped [41, 64] and In-filled [44, 65] CoSb_3 .
282 These values lead to an increase of the maximum PF (Fig. 7c) from about 1
283 $\text{mW m}^{-1} \text{K}^{-2}$ at 400 K for CoSb_3 to 3 and 3.5 $\text{mW m}^{-1} \text{K}^{-2}$ for $\text{Ni}_{0.06}\text{Co}_{0.94}\text{Sb}_3$
284 at 700 K and $\text{In}_{0.13}\text{Co}_4\text{Sb}_{12}$ at 600 K, respectively. The small grain sizes and

285 thus a high concentration of grain boundaries do not seem to alter the sample
 286 transport properties that are dominated by the high crystallinity of the powder
 287 particles.

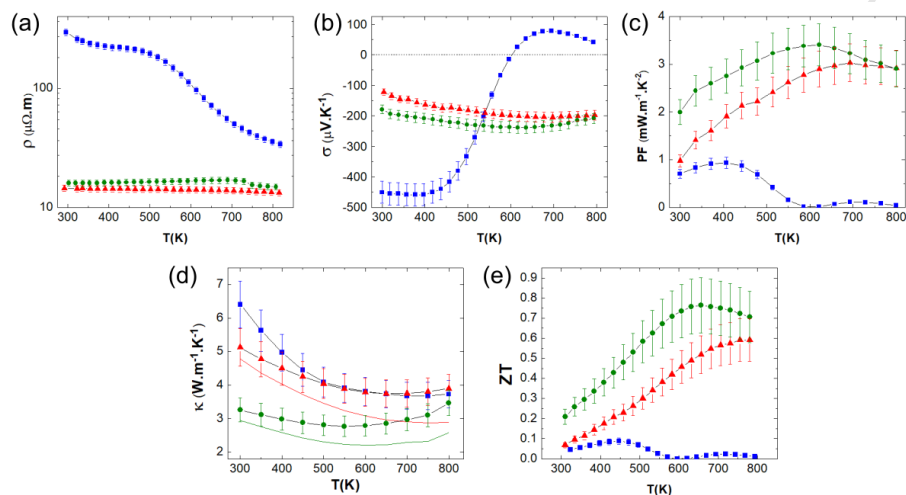


Fig. 7: High-temperature dependence of (a) the electrical resistivity, (b) Seebeck coefficient, (c) power factor, (d) total (symbols) and lattice (solid colored lines) thermal conductivity and (d) figure-of-merit ZT of (■) CoSb_3 , (▲) $\text{Ni}_{0.06}\text{Co}_{0.94}\text{Sb}_3$ and (●) $\text{In}_{0.13}\text{Co}_4\text{Sb}_{12}$. Standard deviations have been estimated to 6 %, 8 %, 13 %, 11 % and 18 % for electrical resistivity, Seebeck coefficient, power factor, thermal conductivity and figure-of-merit ZT , respectively, according to [66]

Table 2: Measured total thermal conductivity and calculated lattice thermal conductivity in $\text{W m}^{-1} \text{K}^{-1}$ of CoSb_3 , $\text{Ni}_{0.06}\text{Co}_{0.94}\text{Sb}_3$ and $\text{In}_{0.13}\text{Co}_4\text{Sb}_{12}$ at 300 K and 800 K compared to the thermal conductivities of macrostructured compounds with similar compositions reported in literature.

	MR samples		Literature data		
	300 K	800 K	300 K	800 K (700 K*)	
CoSb_3	κ	6.5	3.7	11.1 [43], 9.2 [44]	7.5* [43], 4.9 [44]
	κ_L	6.5	3.4	11.1 [43], 9.0 [44]	7.2* [43], 4.6 [44]
$\text{Ni}_{0.06}\text{Co}_{0.94}\text{Sb}_3$	κ	5.1	3.9	6.7 [41]	4.4 [41]
	κ_L	4.7	2.9	6.3 [41]	3.4 [41]
$\text{In}_{0.13}\text{Co}_4\text{Sb}_{12}$	κ	3.3	3.5	3.5 [44], 4.6 [65]	3.0 [44], 3.2* [65]
	κ_L	2.9	2.6	3.1 [44], 3.9 [65]	2.3 [44], 2.5* [65]

288

289 The thermal diffusivity of the three synthesized skutterudites has been mea-
 290 sured on sintered pellets and converted to thermal conductivity (Fig. 7d) using

291 the densities of the pellets and the Dulong and Petit specific heat which usually
 292 applies for skutterudites in this temperature range. The overall shape of $\kappa(T)$
 293 for pristine CoSb_3 corresponds to that usually reported for this material [44].
 294 Nevertheless, it ranges from $6.5 \text{ W m}^{-1} \text{ K}^{-1}$ at 300 K down to $3.7 \text{ W m}^{-1} \text{ K}^{-1}$ at
 295 800 K. Values reported for similar materials which were synthesized by conven-
 296 tional melting-annealing routes and being mostly composed of crystallites much
 297 larger than $1 \mu\text{m}$ are between 9-11 down to 5-7.5 $\text{W m}^{-1} \text{ K}^{-1}$ at 300 K and
 298 700 K, respectively [44, 43, 64]. This corresponds to a reduction of the thermal
 299 conductivity of at least 25 % on the whole temperature range for the metallo-
 300 reduced samples. The here presented values are in better agreement with those
 301 observed for ‘nano’-engineered materials with comparable densities [67, 68].
 302 A direct correlation can be made between the decrease of the thermal conduc-
 303 tivity measured for CoSb_3 and the high concentration of grain boundaries and
 304 associated defects which were evidenced by EBSD/SEM and TEM analyses and
 305 act as efficient phonons scattering centers.

306 Because of the larger electronic contribution to the total thermal conduc-
 307 tivity in the Ni-doped and In-filled samples and to compare more significantly
 308 with literature data, the lattice thermal conductivities κ_L were calculated by
 309 subtracting κ_e to κ_{tot} (Table 2 and solid lines in Fig. 7d). The Wiedmann-Franz
 310 law, $\kappa_e = LT/\rho$, was used to obtain κ_e using the measured electrical resistivity
 311 and a Lorenz number of 1.6×10^{-8} and $1.7 \times 10^{-8} \text{ W } \Omega \text{ K}^{-2}$ for $\text{Ni}_{0.06}\text{Co}_{0.94}\text{Sb}_3$
 312 and $\text{In}_{0.13}\text{Co}_4\text{Sb}_{12}$, respectively [41, 44].

313 The total thermal conductivity of $\text{Ni}_{0.06}\text{Co}_{0.94}\text{Sb}_3$ is 20 % lower than that of
 314 pristine CoSb_3 at 300 K and reaches similar values from 450 up to 800 K. This
 315 reduction of $\kappa(T)$ at room temperature could be explained (i) by the smaller
 316 particle size and thus higher density of grain boundaries and associated de-
 317 fects and (ii) by the higher mass fluctuation on the ‘disordered’ transition metal
 318 sublattice, both enhancing the scattering of phonons and decreasing $\kappa_L(T)$. The
 319 beneficial effect of the mesostructuration is more apparent when κ_L is compared
 320 to the values reported for conventionally synthesized macrostructured materi-
 321 als and where a reduction of $\approx 25 \%$ is noticed at 300 K (Table 2). At higher

322 temperature, the mesostructuration seems to become less and less efficient so
323 that at 800 K the reduction of κ_L falls to $\approx 15\%$. Again, the measured trend
324 and values are in good agreement with reported mesostructured samples with
325 a similar doping level [41, 69].

326 With the insertion of indium rattlers in the structure, the total thermal con-
327 ductivity of $\text{In}_{0.13}\text{Co}_4\text{Sb}_{12}$ is further lowered to 3.2 and 3.5 $\text{W m}^{-1} \text{K}^{-1}$ at 300
328 and 800 K, respectively, with a minimum of 2.8 $\text{W m}^{-1} \text{K}^{-1}$ at about 550 K.
329 These correspond to κ_L of 2.9 $\text{W m}^{-1} \text{K}^{-1}$ at 300 K and 2.6 $\text{W m}^{-1} \text{K}^{-1}$ at 800 K.
330 Comparisons with literature data are rather difficult due to the wide span of
331 (effective) rattler concentration and pellet densities encountered and to the rel-
332 atively large standard deviations inherent to thermal diffusivity measurements.
333 However the presently investigated sample seems to have a slightly lower κ_L than
334 reported value but without strong effect from the mesostructuration opposite to
335 our observations on the two previous compositions. According to Benyahia *et*
336 *al.* [70] who investigated the influence of grain size on $\text{In}_{0.25}\text{Co}_4\text{Sb}_{12}$ lattice
337 thermal conductivity, the reduction of $\kappa_L(T)$ by mesostructuration would have
338 a stronger effect from room temperature to ≈ 580 K while at higher tempera-
339 ture scattering by the rattler would become dominant. This could explain why
340 magnesio-reduced samples have a low κ_L at 300 K compared to those reported
341 in literature but is only in the average at 700 K. Furthermore, in the above
342 mentioned article, a modified Nan and Birringer law [71, 72] was used to es-
343 timate the reduction of κ_L according to the reciprocal of the crystallite size in
344 $\text{In}_{0.25}\text{Co}_4\text{Sb}_{12}$ at 300 K. Applying here this law and considering a mean crystallite
345 size of 600 nm, a reduction of $\kappa_L(300 \text{ K})$ of only $\approx 10\%$ is estimated compared
346 to macrostructured materials. This must be taken as a rough estimate since the
347 synthesis routes and the methods for grain size determination are different, but
348 it would support the reduction of $\kappa_L(T)$ thanks to mesostructuration especially
349 near room temperature in $\text{In}_{0.13}\text{Co}_4\text{Sb}_{12}$.

350 The measured physical properties enable to calculate the figure-of-merit ZT
351 of these materials (Fig. 7e). The ZT values of pristine CoSb_3 are small due to
352 the combined high electrical resistivity and the occurrence of the bipolar effect

353 around 500 K. The obtained values for the Ni-doped and In-filled CoSb_3 increase
354 ZT up to 0.6 at 800 K and 0.75 at 650 K, respectively. In the case of Ni-doped
355 CoSb_3 , this result is very similar to the improved ZT reported for mesostructu-
356 tured $\text{Ni}_{0.06}\text{Co}_{0.94}\text{Sb}_3$ where the reduction of the grain sizes and consequently of
357 the thermal conductivities was realized by high energy ball-milling [69, 41]. In
358 the case of $\text{In}_{0.13}\text{Co}_4\text{Sb}_{12}$, the reduction of κ by mesostructuration is less effec-
359 tive due to the elevated phonon diffusion by In-rattlers and the calculated ZT
360 corresponds well to materials synthesized by conventional melting/annealing
361 methods [43, 44, 65].

362

363 4. Conclusions

364 Pure, Ni-doped and In-filled CoSb_3 were synthesized from metal oxides in only
365 84 h at temperature as low as 810 K by a magnesioreduction process. As-
366 synthesized powders are directly composed of well-crystallized submicronic par-
367 ticles. After spark plasma sintering, pellets with excellent purities and high
368 densities were obtained. XRD and SEM analyses show that the dopant and rat-
369 tler concentrations are very close to the targetted ones, indicating that a good
370 control of the chemical composition is possible with this process. After sinter-
371 ing, the average grain size are found to be 780, 580 and 620 nm for CoSb_3 ,
372 $\text{Ni}_{0.06}\text{Co}_{0.94}\text{Sb}_3$ and $\text{In}_{0.13}\text{Co}_4\text{Sb}_{12}$, respectively. Such small grain size along with
373 the presence of crystal defects and nanoporosity at the grain boundaries were
374 shown to decrease the lattice thermal conductivity of the samples especially for
375 CoSb_3 and $\text{Ni}_{0.06}\text{Co}_{0.94}\text{Sb}_3$ where strong κ_L reduction of 25 % were observed at
376 300 K. The electrical resistivity and Seebeck coefficient measurements show no
377 degradation of the transport properties due to the reduction of grain sizes. This
378 synthesis route thus directly leads to materials approaching the ‘phonon glass-
379 electron crystal’ state [73]. It results in ZT_{max} of 0.09 at 450 K, 0.60 at 800 K and
380 0.75 at 650 K for CoSb_3 , $\text{Ni}_{0.06}\text{Co}_{0.94}\text{Sb}_3$ and $\text{In}_{0.13}\text{Co}_4\text{Sb}_{12}$, respectively. These
381 values are close to those reported in literature for similar compositions but af-
382 ter multistep high temperature syntheses followed by various mesostructura-

383 tion steps. This industrializable process is thus promising for the preparation
384 of thermoelectric materials and will be applied to more complex (multi-doped
385 and -filled) skutterudites but also to other intermetallic thermoelectric materials
386 such as clathrates, (half-)Heusler phases or transition metal silicides.

387 **Acknowledgements**

388 Francis Gouttefangeas is acknowledged for SEM images and EDS analyses per-
389 formed on the CMEBA platform. TEM experiments were performed on THEMIS
390 platform. Both platforms belong to the ScanMAT unit (UMS 2001, University of
391 Rennes 1) which received a financial support from the European Union (CPE-
392 FEDER 2007-2014).// Laura Paradis-Fortin is acknowledged for her careful
393 reading of the article and correction of language errors.

- 394 [1] L. Yang, Z.-G. Chen, M. S. Dargusch, J. Zou, High Performance Thermo-
395 electric Materials: Progress and Their Applications, *Adv. Energy Mater.* 8
396 (2018) 1701797.
- 397 [2] B. C. Sales, D. Mandrus, R. K. Williams, Filled skutterudite antimonides:
398 A new class of thermoelectric materials, *Science* 272 (1996) 1325–1328.
- 399 [3] G. S. Nolas, D. T. Morelli, T. M. Tritt, Skutterudites: A phonon-glass-
400 electron crystal approach to advanced thermoelectric energy conversion
401 applications, *Annu. Rev. Mater. Sci.* 29 (1999) 89–116.
- 402 [4] S. LeBlanc, S. K. Yee, M. L. Scullin, C. Dames, K. E. Goodson, Material
403 and manufacturing cost considerations for thermoelectrics, *Renew. Sust.*
404 *Energ. Rev.* 84 (2014) 313–327.
- 405 [5] G. Rogl, P. Rogl, Skutterudites, a most promising group of thermoelectric
406 materials, *Curr. Opin. Green Sustainable Chem.* 4 (2017) 50–57.
- 407 [6] M. Puyet, C. Candolfi, L. Chaput, V. D. Ros, A. Dauscher, B. Lenoir, J. Hejt-
408 manek, Low-temperature thermal properties of n-type partially filled cal-
409 cium skutterudites, *J. Phys.:Condens. Matter* 18 (2006) 11301–11308.

- 410 [7] G. S. Nolas, J. Yang, H. Takizawa, Transport properties of germanium-
411 filled CoSb_3 , *Appl. Phys. Lett.* 84 (2004) 5210–5212.
- 412 [8] X. Y. Zhao, X. Shi, L. D. Chen, W. Q. Zhang, W. B. Zhang, Y. Z. Pei, Syn-
413 thesis and thermoelectric properties of Sr-filled skutterudite $\text{Sr}_y\text{Co}_4\text{Sb}_{12}$,
414 *J. Appl. Phys.* 99 (2006) 053711.
- 415 [9] G. Rogl, A. Grytsiv, K. Yubuta, S. Puchegger, E. Bauer, C. Raju, R. C.
416 Mallik, P. Rogl, In-doped multifilled n-type skutterudites with $\text{ZT}=1.8$,
417 *Acta Mater.* 95 (2015) 201–211.
- 418 [10] J. Gainza, F. Serrano-Sánchez, J. Prado-Gonjal, N. M. Nemes, N. Biskup,
419 O. J. Dura, J. L. Martínez, F. Fauth, J. A. Alonso, Substantial thermal con-
420 ductivity reduction in mischmetal skutterudites $\text{Mm}_x\text{Co}_4\text{Sb}_{12}$ prepared un-
421 der high-pressure conditions, due to uneven distribution of the rare-earth
422 elements, *J. Mater. Chem. C* 7 (2019) 4124–4131.
- 423 [11] K. Wojciechowski, J. Tobola, J. Leszczynski, Thermoelectric properties and
424 electronic structure of CoSb_3 doped with Se and Te, *J. Alloys Compd.* 361
425 (2003) 19–27.
- 426 [12] J. Mi, X. Zhao, T. Zhu, J. Ma, Thermoelectric properties of skutterudites
427 $\text{Fe}_x\text{Ni}_y\text{Co}_{1-x-y}\text{Sb}_3$ ($x=y$), *J. Alloys Compd.* 452 (2008) 225–229.
- 428 [13] Y. Lan, A. J. Minnich, G. Chen, Z. Ren, Enhancement of Thermoelectric
429 Figure-of-Merit by a Bulk Nanostructuring Approach, *Adv. Funct. Mater.*
430 20 (2010) 357–376.
- 431 [14] X. Meng, Z. Liu, B. Cui, D. Qin, H. Geng, W. Cai, L. Fu, J. He, Z. Ren, J. Sui,
432 Grain Boundary Engineering for Achieving High Thermoelectric Perfor-
433 mance in n-Type Skutterudites, *Adv. Energy Mater.* 7 (2017) 1602582.
- 434 [15] G. Joshi, H. Lee, Y. Lan, X. Wang, G. Zhu, D. Wang, R. W. Gould, D. C. Cuff,
435 M. Y. Tang, M. S. Dresselhaus, G. Chen, Z. Ren, Enhanced Thermoelectric
436 Figure-of-Merit in Nanostructured p-type Silicon Germanium Bulk Alloys,
437 *Nano Lett.* 8 (2008) 4670–4674.

- 438 [16] L. Yang, Z. G. Chen, M. Hong, G. Han, J. Zou, Enhanced Thermoelectric
439 Performance of Nanostructured Bi₂Te₃ through Significant Phonon Scat-
440 tering, ACS Appl. Mater. Interfaces 7 (2015) 23694–23699.
- 441 [17] C. Recknagel, N. Reinfried, P. Höhn, W. Schnelle, H. Rosner, Y. Grin,
442 A. Leithe-Jasper, Application of spark plasma sintering to the fabrication of
443 binary and ternary skutterudites, Sci. Tech. Adv. Mater. 8 (2007) 357–363.
- 444 [18] V. Trivedi, M. Battabyal, P. Balasubramanian, G. M. Muralikrishna, P. K.
445 Jain, R. Gopalan, Microstructure and doping effect on the enhancement
446 of the thermoelectric properties of Ni doped Dy filled CoSb₃ skutterudites,
447 Sustain. Energ. Fuels 2 (2018) 2687–2697.
- 448 [19] G. Rogl, A. Grytsiv, R. Anbalagan, J. Bursik, M. Kerber, E. Schafler, M. Ze-
449 hetbauer, E. Bauer, P. Rogl, Direct SPD-processing to achieve high-ZT skut-
450 terudites, Acta Mater. 159 (2018) 352–363.
- 451 [20] L. Guo, G. Wang, K. Peng, Y. Yan, X. Tang, M. Zeng, J. Dai, G. Wangand,
452 X. Zhou, Melt spinning synthesis of p-type skutterudites: Drastically speed
453 up the process of high performance thermoelectrics, Scripta Mater. 116
454 (2016) 26–30.
- 455 [21] S. Lee, K. H. Lee, Y.-M. Kim, H. S. Kim, G. J. Snyder, S. Baik, S. W. Kim,
456 Simple and efficient synthesis of nanograin structured single phase filled
457 skutterudite for high thermoelectric performance, Acta. Mater. 142 (2018)
458 8–17.
- 459 [22] E. Godlewska, K. Mars, K. Zawadzka, Alternative route for the preparation
460 of CoSb₃ and Mg₂Si derivatives, J. Solid State Chem. 193 (2012) 109–113.
- 461 [23] F. Gucci, T. G. Saunders, M. J. Reece, In-situ synthesis of n-type un-
462 filled skutterudite with reduced thermal conductivity by hybrid flash-spark
463 plasma sintering, Scripta Mater. 157 (2018) 58–61.
- 464 [24] L. Kong, X. Jia, Y. Zhang, B. Sun, B. Liu, H. Liu, C. Wang, B. Liu, J. Chen,
465 H. Ma, N-type Ba_{0.3}Ni_{0.15}Co_{3.85}Sb₁₂ skutterudite: High pressure processing

- 466 technique and thermoelectric properties, *J. Alloys Compd.* 734 (2018) 36–
467 42.
- 468 [25] L. Deng, J. Ni, L. Wang, X. Jia, J. Qin, B. Liu, Structure and thermoelectric
469 properties of $\text{In}_x\text{Ba}_y\text{Co}_4\text{Sb}_{12}$ samples prepared by HPHT, *J. Alloys Compd.*
470 712 (2017) 477–481.
- 471 [26] A. Sesselmann, G. Skomedal, H. Middleton, E. Müller, The Influence of
472 Synthesis Procedure on the Microstructure and Thermoelectric Proper-
473 ties of p-Type Skutterudite $\text{Ce}_{0.6}\text{Fe}_2\text{Co}_2\text{Sb}_{12}$, *J. Electron. Mater.* 45 (2015)
474 1397–1407.
- 475 [27] M. S. Toprak, C. Stiewe, D. Platzek, S. Williams, L. Bertini, E. Müller,
476 C. Gatti, Y. Zang, M. Rowe, M. Muhammed, The impact of nanostruc-
477 turing on the thermal conductivity of thermoelectric CoSb_3 , *Adv. Funct.*
478 *Mater.* 14 (2004) 1189–1196.
- 479 [28] Y. Li, C. Li, B. Wang, W. Li, P. Che, A comparative study on the thermo-
480 electric properties of CoSb_3 prepared by hydrothermal and solvothermal
481 route, *J. Alloys Compd.* 772 (2019) 770–774.
- 482 [29] K. Biswas, J. He, I. D. Blum, C.-I. Wu, T. P. Hogan, D. N. Seidman, V. P.
483 Dravid, M. G. Kanatzidis, High-performance bulk thermoelectrics with all-
484 scale hierarchical architectures, *Nature* 489 (2012) 414–418.
- 485 [30] X. Meng, Z. Liu, B. Cui, D. Gin, H. Geng, W. Cai, L. Fu, J. He, Z. Ren,
486 J. Sui, Grain Boundary Engineering for Achieving High Thermoelectric Per-
487 formance in n-Type Skutterudite, *Adv. Energy Mater.* 7 (2017) 642–651.
- 488 [31] W. Li, J. Wang, Y. Xie, J. L. Gray, J. J. Heremans, H. B. Kang, B. Poudel,
489 S. T. Huxtable, S. Priya, Enhanced thermoelectric performance of Yb-
490 single-filled skutterudite by ultralow thermal conductivity, *Chem. Mater.*
491 31 (2019) 862–872.

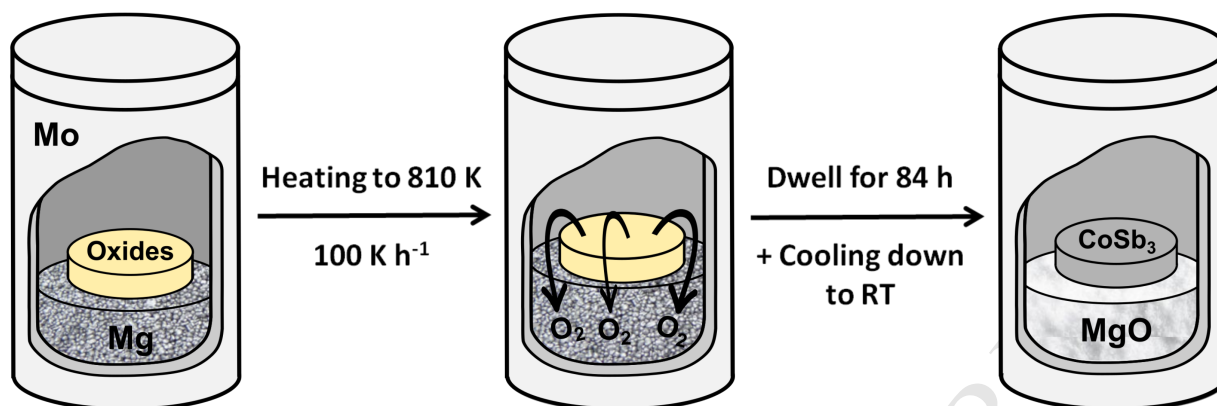
- 492 [32] G. Rogl, A. Grytsiv, P. Rogl, E. Bauer, M. B. Kerber, M. Zehetbauer,
493 S. Puchegger, Multifilled nanocrystalline p-type didymium-Skutterudites
494 with $ZT > 1.2$, *Intermetallics* 18 (2010) 2435–2444.
- 495 [33] M. Matsubara, Y. Masuoka, R. Asahi, Effects of doping IIIB elements (Al,
496 Ga, In) on thermoelectric properties of nanostructured n-type filled skutterudite
497 compounds, *J. Alloys Compd.* 774 (2019) 731–738.
- 498 [34] H. Yang, P. Wen, X. Zhou, Y. Li, B. Duan, P. Zhai, Q. Zhang, Enhanced ther-
499 moelectric performance of Te-doped skutterudite with nano-micro-porous
500 architecture, *Scripta Mater.* 159 (2018) 68–71.
- 501 [35] A. U. Khan, K. Kobayashi, D.-M. Tang, Y. Yamauchi, K. Hasegawa, M. Mit-
502 ome, Y. Xue, B. Jiang, K. Tsuchiya, D. Golberg, Y. Bando, T. Mori, Nano-
503 micro-porous skutterudites with 100% enhancement in ZT for high per-
504 formance thermoelectricity, *Nano Energy* 31 (2017) 152–159.
- 505 [36] H. Li, X. Su, X. Tang, Q. Zhang, C. Uher, G. J. Snyder, U. Aydemir,
506 Grain boundary engineering with nano-scale InSb producing highper-
507 formance $\text{In}_x\text{Ce}_y\text{Co}_4\text{Sb}_{12+z}$ skutterudite thermoelectrics, *J. Materiomics* 3
508 (2017) 273–279.
- 509 [37] P. Chen, Z. Zhou, W. Jiang, Wei Luo, J. Yang, J. Zhu, L. Wang, Y. Fan, En-
510 hancing the thermoelectric performance of filled skutterudite nanocom-
511 posites in a wide temperature range via electroless silver plating, *Scripta*
512 *Mater.* 146 (2018) 136–141.
- 513 [38] H. Zhao, B. Cao, S. Li, N. Liu, J. Shen, S. Li, J. Jian, L. Gu, Y. Pei, G. J.
514 Snyder, Z. Ren, X. Chen, Engineering the Thermoelectric Transport in Half-
515 Heusler Materials through a Bottom-Up Nanostructure Synthesis, *Adv. En-*
516 *ergy Mater.* 7 (2017) 1700446.
- 517 [39] L. Ma, C. Y. Seo, X. Chen, K. Sun, J. W. Schwank, Indium-doped Co_3O_4
518 nanorods for catalytic oxidation of CO and C_3H_6 towards diesel exhaust,
519 *Appl. Catal. B-Environ.* 222 (2018) 44–58.

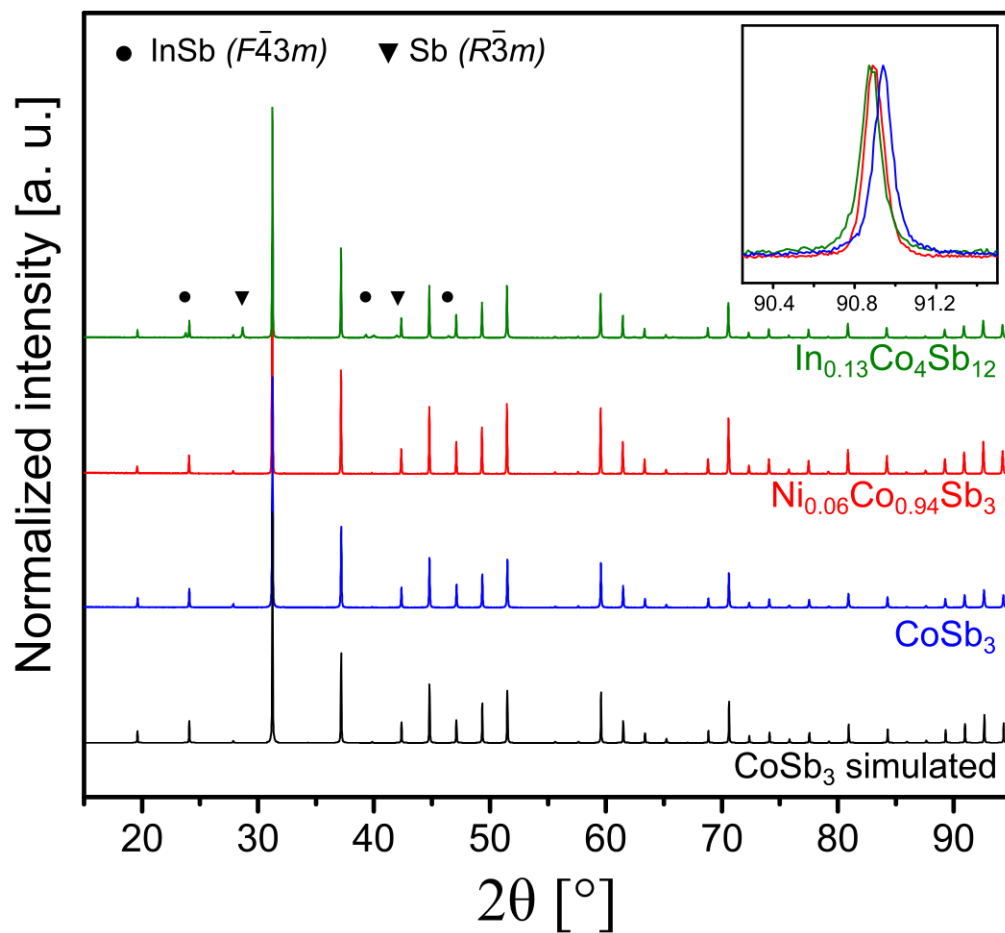
- 520 [40] E. Alleno, E. Zehani, O. Rouleau, Metallurgical and thermoelectric prop-
521 erties in $\text{Co}_{1-x}\text{Pd}_x\text{Sb}_3$ and $\text{Co}_{1-x}\text{Ni}_x\text{Sb}_3$ revisited, *J. Alloys Compd.* 572
522 (2013) 43–48.
- 523 [41] E. Alleno, E. Zehani, M. Gaborit, V. Orodniichuk, B. Lenoir, M. Benyahia,
524 Mesostructured thermoelectric $\text{Co}_{1-y}\text{M}_y\text{Sb}_3$ (M = Ni, Pd) skutterudites, *J.*
525 *Alloys Compd.* 692 (2017) 676–686.
- 526 [42] T. He, J. Chen, H. D. Rosenfeld, M. A. Subramanian, Thermoelectric prop-
527 erties of indium-filled skutterudites, *Chem. Mater.* 18 (2006) 759–762.
- 528 [43] R. C. . Mallik, J. Y. Jung, S. C. Ur, I. H. Kim, Thermoelectric properties of
529 $\text{In}_z\text{Co}_4\text{Sb}_{12}$ skutterudites, *Met. Mater. Int.* 14 (2008) 223–228.
- 530 [44] J. Leszczynski, V. D. Ros, B. Lenoir, A. Dauscher, C. Candolfi, P. Mass-
531 chelein, J. Hejtmanek, K. Kutorasinski, J. Tobola, R. I. Smith, C. Stiewe,
532 E. Müller, Electronic band structure, magnetic, transport and thermody-
533 namic properties of In-filled skutterudites $\text{In}_x\text{Co}_4\text{Sb}_{12}$, *J. Phys. D: Appl.*
534 *Phys.* 46 (2013) 495106.
- 535 [45] R. C. Mallik, C. Stiewe, G. Karpinski, R. Hassdorf, E. Müller, Thermoelec-
536 tric properties of $\text{Co}_4\text{Sb}_{12}$ skutterudite materials with partial In filling and
537 excess In additions, *J. Electron. Mater.* 38 (2009) 1337–1339.
- 538 [46] G. Li, K. Kurosaki, Y. Ohishi, H. Muta, S. Yamanaka, Thermoelectric prop-
539 erties on Indium-added skutterudites $\text{In}_x\text{Co}_4\text{Sb}_{12}$, *J. Electron. Mater.* 42
540 (2013) 1463–1468.
- 541 [47] E. Visnow, C. P. Heinrich, A. S. and J. de Boor, P. Leidich, B. Klobes, R. P.
542 Hermann, W. E. Müller, W. Tremel, On the true Indium content on In-filled
543 skutterudites, *Inorg. Chem.* 54 (2015) 7818–7827.
- 544 [48] J. Rodriguez-Carvajal, Recent advances in magnetic-structure determina-
545 tion by neutron powder diffraction, *Physica B* 192 (1993) 55–69.

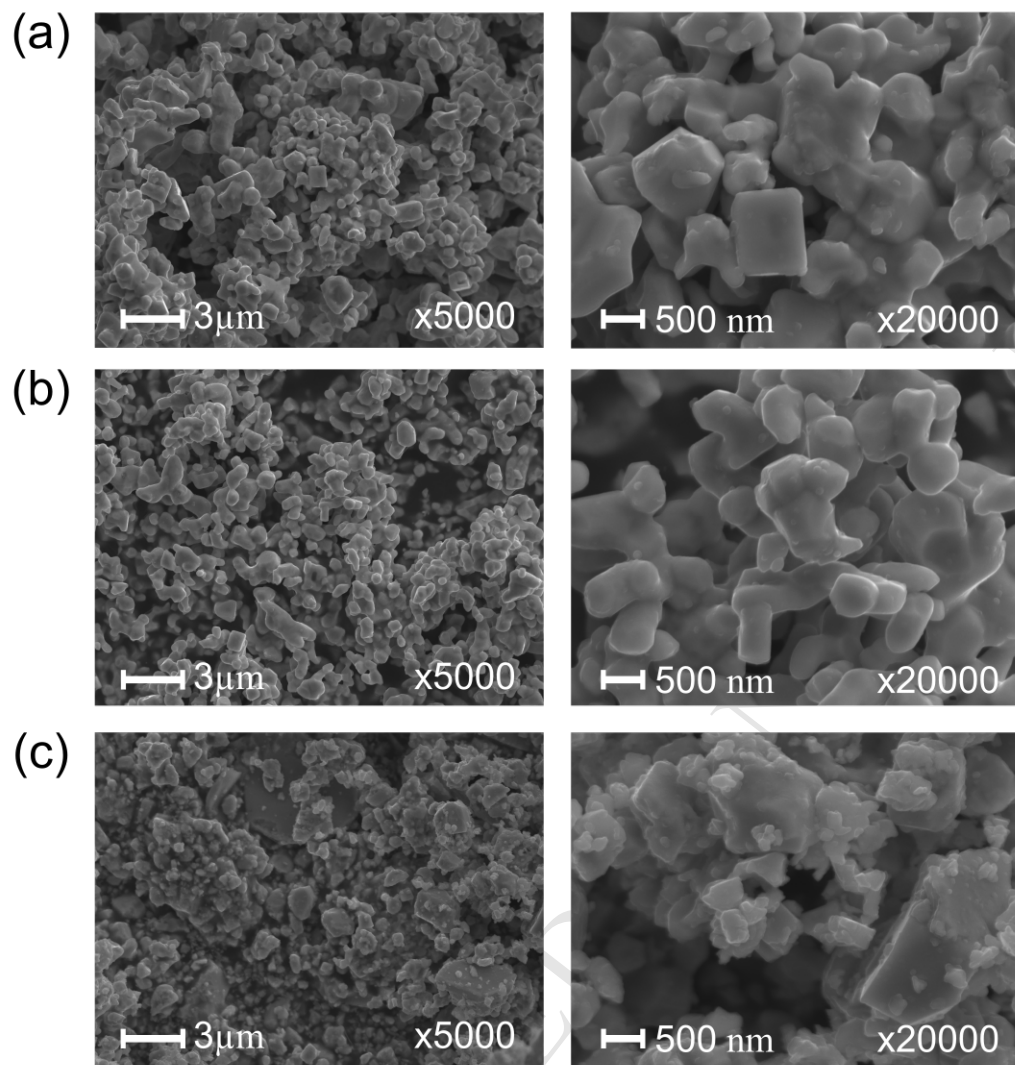
- 546 [49] O. Rouleau, E. Alleno, Measurement system of the Seebeck coefficient or of
547 the electrical resistivity at high temperature, *Rev. Sci. Instrum.* 84 (2013)
548 105103.
- 549 [50] D. G. Mandrus, A. Migliori, T. W. Darling, M. F. Hundley, E. J. Peterson,
550 J. D. Thompson, Electronic transport in lightly doped CoSb_3 , *Phys. Rev. B*
551 52 (1995) 4926–4931.
- 552 [51] M. Christensen, B. B. Iversen, L. Bertini, C. Gatti, M. Toprak,
553 M. Muhammed, E. Nishibori, Structural study of Fe doped and Ni substi-
554 tuted thermoelectric skutterudites by combined synchrotron and neutron
555 powder diffraction and *ab initio* theory, *J. Appl. Phys.* 96 (2004) 3148–
556 3157.
- 557 [52] W. Zhao, P. Wei, Q. J. Zhang, H. Peng, W. T. Zhu, D. G. Tang, J. Yu,
558 H. Y. Zhou, Z. Y. Liu, X. Mu, D. Q. He, J. C. Li, C. L. Wang, X. F. Tang,
559 J. H. Yang, Multi-localization transport behaviour in bulk thermoelectric
560 materials, *Nat. Commun.* 6 (2015) 6197.
- 561 [53] A. Grytsiv, P. Rogl, H. Michor, E. Bauer, G. Giester, $\text{In}_y\text{Co}_4\text{Sb}_{12}$ Skutteru-
562 dite: Phase Equilibria and Crystal Structure, *J. Electron. Mater.* 42 (2013)
563 2940–2952.
- 564 [54] G. Champion, J. Allenou, M. Pasturel, H. Noël, F. Charollais, M. Anselmet,
565 X. Iltis, O. Tougait, Magnesiothermic Reduction Process Applied to the
566 Powder Production of U(Mo) Fissile Particles, *Adv. Eng. Mater.* 15 (2013)
567 257–261.
- 568 [55] K. Choi, H. Choi, H. Na, I. Sohn, Effect of magnesium on the phase equi-
569 libria in magnesio-thermic reduction of Nb_2O_5 , *Mater. Lett.* 183 (2016)
570 151–155.
- 571 [56] C. Won, H. Nersisyan, H. Won, Titanium powder prepared by a rapid
572 exothermic reaction, *Chem. Eng. J.* 157 (2010) 270–275.

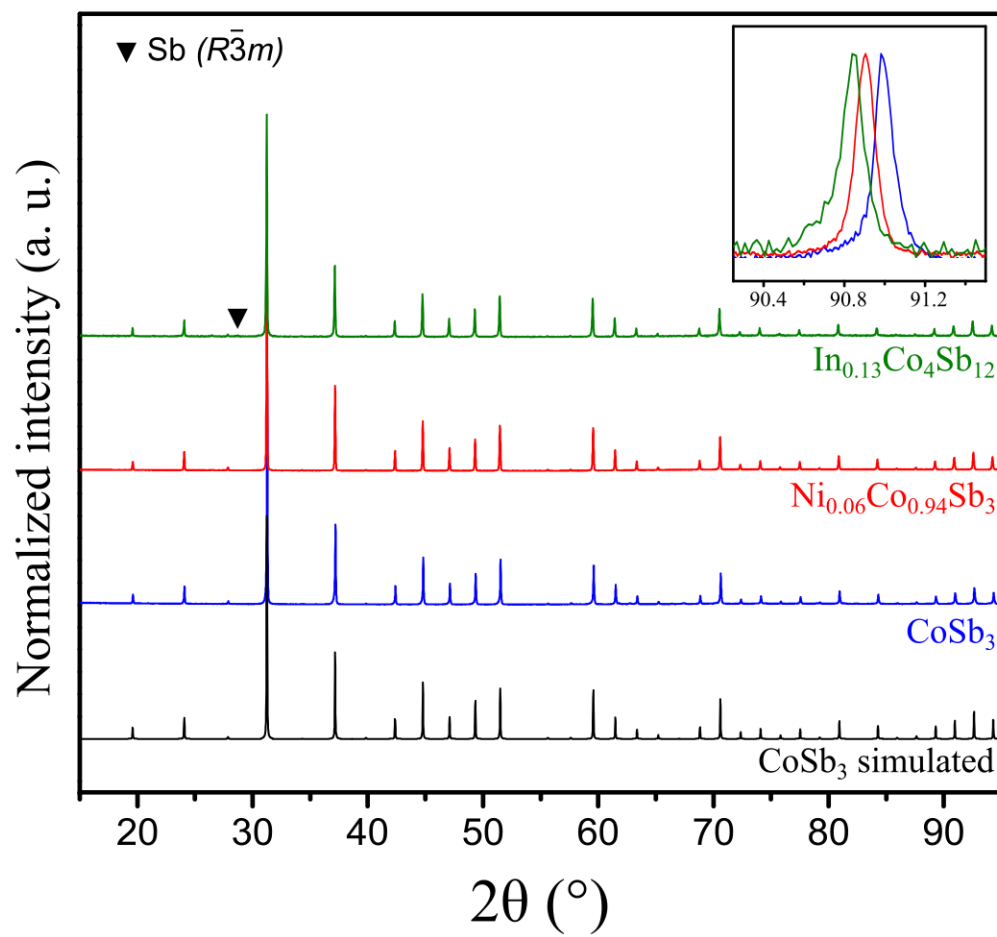
- 573 [57] H. J. T. Ellingham, Reducibility of oxides and sulfides in metallurgical
574 processes, *J. Soc. Chem. Ind.* 63 (1944) 125–160.
- 575 [58] R. C. Sharma, T. L. Ngai, Y. A. Chang, The In-Sb (Indium-Antimony) sys-
576 tem, *Bull. Alloy Phase Diagrams* 10 (1989) 657–664.
- 577 [59] G. Rogl, A. Grytsiv, P. Rogl, E. Royanian, E. Bauer, J. Horky, D. Setman,
578 E. Schafner, M. Zehetbauer, Dependence of thermoelectric behaviour on
579 severe plastic deformation parameters: A case study on p-type skutteru-
580 dide $\text{DD}_{0.60}\text{Fe}_3\text{CoSb}_{12}$, *Acta. Mater.* 61 (2013) 6778–6789.
- 581 [60] L. Yang, J. Wu, L. Zhang, Synthesis of filled skutterudite compound
582 $\text{La}_{0.75}\text{Fe}_3\text{CoSb}_{12}$ by spark plasma sintering and effect of porosity on ther-
583 moelectric properties, *J. Alloys Compd.* 364 (2004) 83–88.
- 584 [61] J. Friedel, *Dislocations*, 1st Edition, Pergamon Press, 1964 (1964).
- 585 [62] Y. Kawaharada, K. Kurosaki, M. Uno, S. Yamanaka, Thermoelectric prop-
586 erties of CoSb_3 , *J. Alloys Compd.* 315 (2001) 193–197.
- 587 [63] J. W. Sharp, E. C. Jones, R. K. Williams, P. M. Martin, B. C. Sales, Thermo-
588 electric properties of CoSb_3 and related alloys, *J. Appl. Phys.* 78 (1995)
589 1013–1018.
- 590 [64] H. Kitagawa, M. Wakatsuki, H. Nagaoka, H. Noguchi, Y. Isoda,
591 K. Hasezaki, Y. Noda, Temperature dependence of thermoelectric prop-
592 erties of Ni-doped CoSb_3 , *J. Phys. Chem. Solid.* 66 (2005) 1635–1639.
- 593 [65] A. Sesselmann, B. Klobes, T. Dasgupta, O. Gourdon, R. Hermann,
594 E. Müller, Neutron diffraction and thermoelectric properties of in-
595 dium filled $\text{In}_x\text{Co}_4\text{Sb}_{12}$ ($x=0.05, 0.2$) and indium cerium filled
596 $\text{Ce}_{0.05}\text{In}_{0.1}\text{Co}_4\text{Sb}_{12}$ skutterudites, *Phys. Stat. Sol. A* 213 (2016) 766–773.
- 597 [66] E. Alleno, D. Berardan, C. Bly, C. Candolfi, R. Daou, R. Decourt,
598 E. Guilmeau, S. Hebert, J. Hejtmanek, B. Lenoir, P. Masschelein,
599 V. Ohorodnichuk, M. Pollet, S. Populoh, D. Ravot, O. Rouleau, M. Soulier,

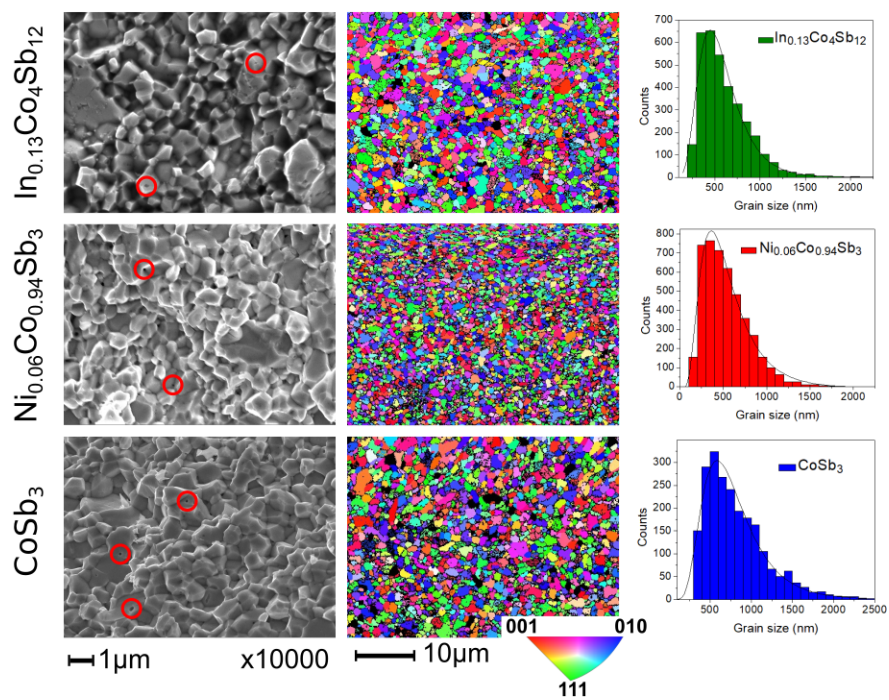
- 600 A round robin test of the uncertainty on the measurement of the thermo-
601 electric dimensionless figure of merit of $\text{Co}_{0.97}\text{Ni}_{0.03}\text{Sb}_3$, *Rev. Sci. Instrum.*
602 86 (2015) 011301.
- 603 [67] E. Alleno, L. Chen, Chubilleau, B. Lenoir, O. Rouleau, M. Trichet,
604 B. Villeroy, Thermal Conductivity Reduction in CoSb_3 - CeO_2 Nanocompos-
605 ites, *J. Electron. Mater.* 39 (2010) 1966–1970.
- 606 [68] A. Khan, M. Saleemi, M. Johnsson, L. Han, N. Nong, M. Muhammed,
607 M. Toprak, Fabrication, spark plasma consolidation, and thermoelectric
608 evaluation of nanostructured CoSb_3 , *J. Alloys Compd.* 612 (2014) 293–
609 300.
- 610 [69] Q. He, Q. Hao, X. Wang, J. Yang, Y. Lan, X. Yan, B. Yu, Y. Ma, B. Poude,
611 G. Joshi, D. Wang, G. Chen, Z. Ren, Nanostructured Thermoelectric Skut-
612 terudite $\text{Co}_{1-x}\text{Ni}_x\text{Sb}_3$ Alloys, *J. Nanosci. Nanotechnol.* 8 (2008) 4003–
613 4006.
- 614 [70] M. Benyahia, V. Ohorodniichuk, E. Leroy, A. Dauscher, B. Lenoir, E. Alleno,
615 High thermoelectric figure of merit in mesostructured $\text{In}_{0.25}\text{Co}_4\text{Sb}_{12}$ n-type
616 skutterudite, *J. Alloys Compd.* 735 (2018) 1096–1104.
- 617 [71] C. W. Nan, R. Birringer, Determining the Kapitza resistance and the ther-
618 mal conductivity of polycrystals: A simple model, *Phys. Rev. B* 14 (1998)
619 8264–8268.
- 620 [72] H. S. Yang, G. Bai, L. Thompson, J. Eastman, Interfacial thermal resistance
621 in nanocrystalline yttria-stabilized zirconia, *Acta Mater.* 50 (2002) 2309–
622 2317.
- 623 [73] G. A. Slack, Design Concepts for Improved Thermoelectric Materials, *MRS*
624 *Proceedings* 478 (1997) 47.

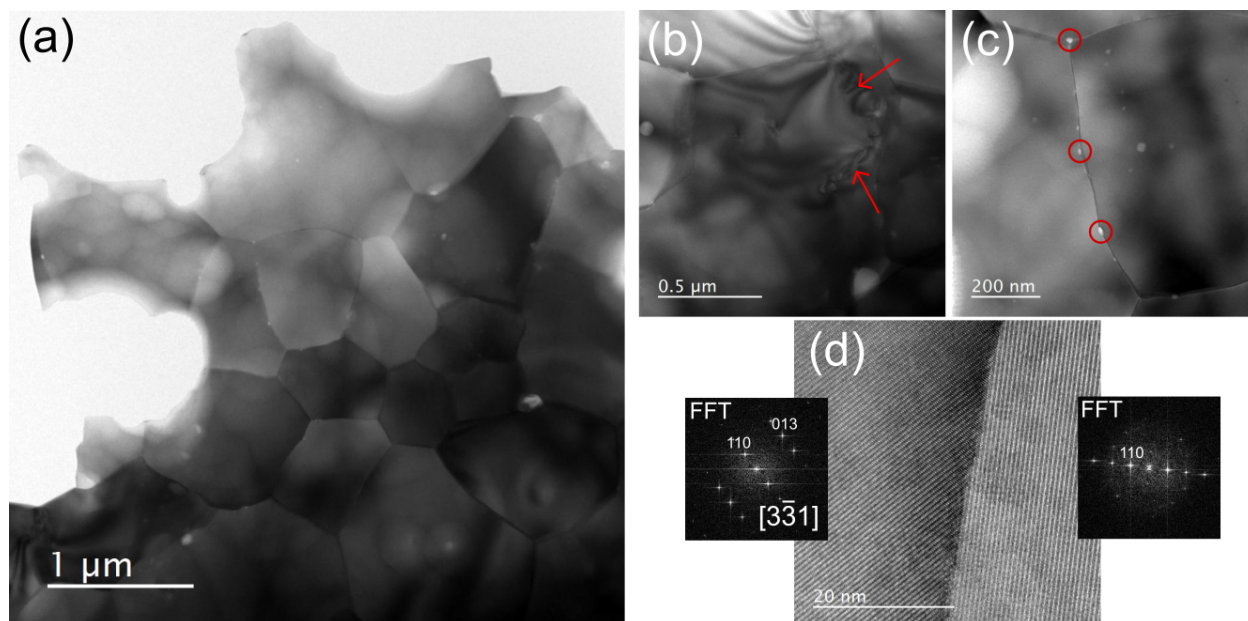




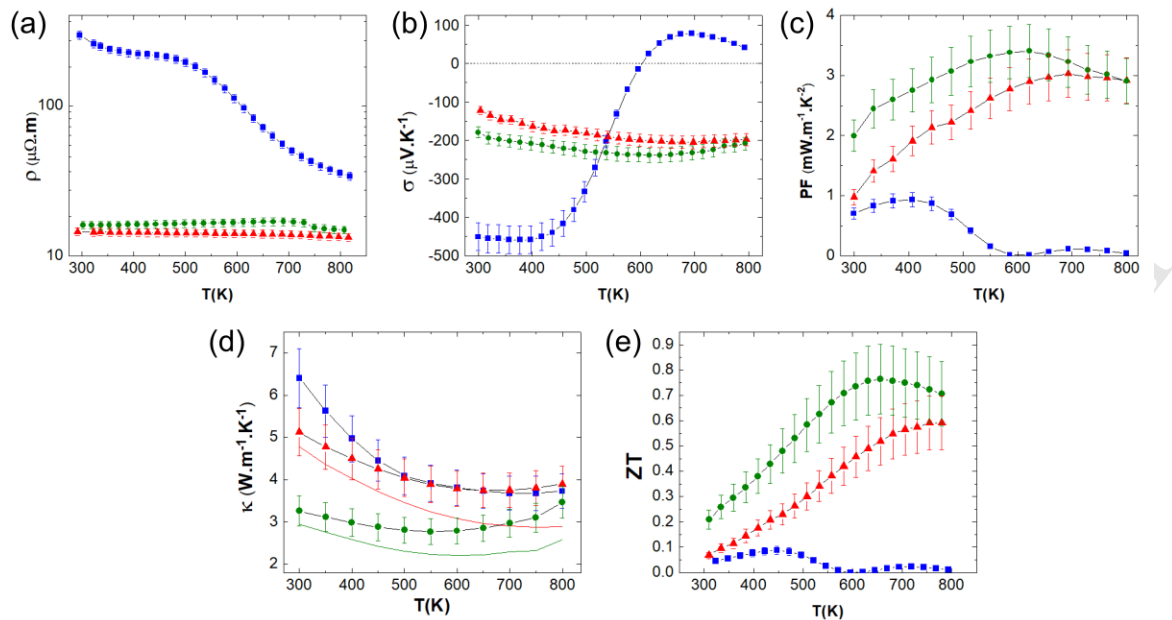








ACCEPTED MANUSCRIPT



- Magnesio-reduction of oxides is used to prepare skutterudites.
- Well-crystallized and submicronic powders are obtained at low temperature.
- The mesostructure survives after spark plasma sintering.
- Accordingly, improved thermoelectric performances are achieved.
- Thermoelectric properties are discussed toward microstructure of the materials.

ACCEPTED MANUSCRIPT